

Investigating the effect of defects on the crack initiation of additively manufactured IN718 using crystal plasticity simulations

Indrajit Nandi^{1,2}, Nima Shamsaei^{1,2}, Shuai Shao^{1,2*}

¹ National Center for Additive Manufacturing Excellence (NCAME), Auburn University, Auburn, AL 36849, USA

² Department of Mechanical Engineering, Auburn University, Auburn, AL 36849, USA

*Corresponding author: sshao@auburn.edu
Phone: (334) 844-4867

Abstract

This study aims to analyze the effect of defects location on the fatigue behavior of additively manufactured IN718. A competing mechanism exists between persistent slip bands (PSBs) and volumetric defects on the initiation of fatigue cracks in AM IN718 under cyclic loading. Crystal plasticity simulations were performed to reveal the relative importance in crack initiation due to defects and PSBs. Cyclic loading was applied on a defect laden polycrystalline aggregate and the defect locations were systematically varied. The crack nucleation cycles and locations were captured using a strain contrast-based crack initiation criterion. The findings suggest that the presence of large defects affects the cyclic strain localization and crack initiation behavior of the AM IN718 material.

Keywords: Additive manufacturing; Crystal plasticity simulation; IN718; Defects.

Introduction

IN718 is a nickel-based superalloy that finds application in the aerospace industry, commonly in gas turbines and rocket engines, for its high temperature strength, corrosion, and creep-rupture resistance. It is a γ - γ' - γ'' precipitation hardened superalloy with face-centered cubic (FCC) matrix lattice structure. IN718 typically suffers from poor machinability due to its high hardness and wear resistance. The high cost of machining and good weldability makes IN718 an attractive alloy for additive manufacturing (AM). Laser powder bed fusion (L-PBF) is a popular AM method to fabricate complex near-net-shape components with precise dimension. Although L-PBF is a promising technology, the manufactured parts contain large population of volumetric defects such as gas entrapped pores, lack of fusion, and keyholes. The defects act as stress risers and can compromise the mechanical properties of the AM parts especially fatigue behavior.

Fatigue crack does not always initiate from volumetric defects in IN718, and the material appears less susceptible to defects than other alloys [1]. Often fatigue crack initiation sites are identified on the fracture surfaces as crystallographic facets [2], which has been attributed to the formation and operation of persistent slip bands (PSBs) along the crystallographic slip planes. Wan et al. [3] reported gas entrapped pores as the main fatigue crack initiator at the mid and high cycle fatigue (MCF and HCF) regimes, while Yang et al. [4] observed both volumetric defects and facets as the crack initiator in the HCF and very high cycle fatigue regimes. A recent study by Muhammad et al. [5] on the L-PBF IN718 specimens showed crystallographic facets larger than 100 μm in diameter as the crack initiator despite the presence of large defects of $\sim 40 \mu\text{m}$ in diameter. This portrays a competing mechanism between facet- and defect- driven crack initiation in surface machined AM IN718 under fatigue loading.

Dodaran et al. [6] performed crystal plasticity (CP) simulations and experimental analysis, and investigated the competition between defects and PSBs on the crack initiation of AM IN718. Very small defects compared to FSD didn't affect strain localization and crack initiation behavior. Dodaran et al. [6] fixed the location of defects and only changed the defect size. So, the location effect of defects in AM material is still uncertain. As the population of defects are high in AM IN718, the location of the large volumetric defects can be critical and can affect the fatigue behavior of the material.

The present study aims to fill the knowledge gap in understanding how the location of volumetric defects affects the crack initiation mechanism of AM IN178 material. In this work, cyclic loading on a defect-laden polycrystalline aggregate has been modeled using CP simulations. A physics-based CP slip strength evolution law, and crack initiation criteria based on strain contrast proposed by Dodaran et al. [6] have been employed to investigate the competing fatigue crack initiation mechanism between PSBs and defects. The location of the defects is varied systematically to understand the effect of defect location on the crack initiation mechanism.

Computational Methodology

CP simulations were performed in a finite-strain continuum mechanical framework using the Düsseldorf Advanced Material Simulation Kit (DAMASK) developed by Max-Planck-Institut für Eisenforschung [7]. A FSD-based material strength model developed by Dodaran et al. [6], which are compatible with the CP framework, was used with the fast Fourier transform-based spectral solver to perform the CP simulations in DAMASK. The material parameters were obtained from Dodaran et al. [6], where virtual single crystal simulations were performed by calibrating with the experimental data for both tensile and fatigue loading conditions. Isotropic plasticity with very low material strength properties was used to model the behavior of volumetric defects (pores) as shown in Table 1. While the details of the crystal plasticity formulation followed in this study had been described in the work of Dodaran et al. [6], key equations where the parameters presented in Table 1 are still introduced below.

The flow rule that has been used to define the shear rate ($\dot{\gamma}_\alpha$) of the material is:

$$\dot{\gamma}_\alpha = \dot{\gamma}_0 \left| \frac{\tau_\alpha - \chi_\alpha}{\xi_\alpha} \right|^{1/m} \text{sgn}(\tau_\alpha - \chi_\alpha) \quad (1)$$

here $\dot{\gamma}_0$ is the reference rate of the shear strain, τ_α is the resolved shear stress, χ_α is the back stress, ξ_α is the slip resistance for slip system α , and m is the strain rate sensitivity. The initial and final slip resistances are expressed as:

$$\xi_\alpha^{ini} = \xi_\alpha^{ini_0} + k / \sqrt{\eta_\alpha}, \quad \xi_\alpha^{sat} = \xi_\alpha^{sat_0} + k / \sqrt{\eta_\alpha} \quad (2)$$

here k is the Hall-Petch parameter, ξ_α^{ini} and ξ_α^{sat} are the initial and saturation slip resistances on system α , and $\xi_\alpha^{ini_0}$ and $\xi_\alpha^{sat_0}$ are the reference initial and saturation slip resistances. The Armstrong and Fredrick model was used to design the evolution of back stress during cyclic loading as:

$$\dot{\chi}_\alpha = u\dot{\gamma}_\alpha - r\chi_\alpha|\dot{\gamma}_\alpha| \quad (3)$$

here u is the hardening coefficient and r is the dynamic recovery parameter. The location-dependent evolution rate of the slip resistance can be defined as:

$$\dot{\xi}_\alpha = \sum_{\alpha'=1}^{N_s} h_{\alpha\alpha'} |\dot{\gamma}_{\alpha'}| \left| 1 - \frac{\xi_{\alpha'}}{\xi_{\alpha}^{sat}} \right|^a \text{sgn} \left(1 - \frac{\xi_{\alpha'}}{\xi_{\alpha}^{sat}} \right) \text{sgn}(\eta_\alpha - \lambda) \quad (4)$$

here λ is the FSD threshold parameter.

The flow rule for the isotropic elasto-plastic material model used to define the volumetric defects (pores) are expressed as:

$$\dot{\gamma}_p = \dot{\gamma}_0 \left(\frac{\sqrt{3}J_2}{T\omega} \right)^q \quad (5)$$

where J_2 is the second invariant of the Mandel stress tensor (M_p), T is the Taylor factor, q is the stress exponent, and ω denotes the scalar resistance to plastic flow. The evolution of the resistance parameter (ω) is defined by:

$$\dot{\omega} = \dot{\gamma} h_0 \left| 1 - \frac{\omega}{\omega^{sat}} \right|^a \text{sgn} \left(1 - \frac{\omega}{\omega^{sat}} \right) \quad (6)$$

here h_0 is the initial hardening parameter, ω^{sat} is the saturation resistance, and a is the strain rate sensitivity exponent. Here C_{11} , C_{12} , and C_{44} are the components of the elastic stiffness matrix.

Table 1. Material constants used in the CP simulations for IN718: elastic and plastic constants adopted from the literature ([6–8]).

Elastic and plastic constants for materials													
C_{11} (GPa)	C_{12} (GPa)	C_{44} (GPa)	$\dot{\gamma}_0$ (s ⁻¹)	m	u (MPa)	r	$\dot{\chi}_0$ (MPa·s ⁻¹)	$\xi_\alpha^{ini_0}$ (MPa)	$\xi_\alpha^{sat_0}$ (MPa)	a	h_0^{s-s}	k (MPa)	λ (μm)
259.6	179.0	109.6	0.007	0.13	39.0	0.4	10.0	300.0	100.0	1.0	100.0	0.4	40.0
Elastic and plastic constants for pores													
C_{11} (GPa)	C_{12} (GPa)	C_{44} (GPa)	$\dot{\gamma}_0$ (s ⁻¹)	T (MPa)	a	q (MPa)	ω^{ini} (MPa)	ω^{sat} (MPa)	h_0 (MPa)				
259.6	179.0	109.6	0.01	20	2.5	4.0	0.02	0.5	0.075				

Model Setup

Figure 1 presents the polycrystalline model geometry used in the CP simulation, adopted from Dodaran et al. [6]. The representative volume element (RVE) consists of 24 grains with the central one being larger and 23 smaller grains of uniform sizes surrounding it as neighbors. Volumetric defects were incorporated in the large central grain of the RVE. The physical appearance of the RVE is cubic in shape and 115 μm in edge length. The grains were discretized by a 33 (X) x 33 (Y) x 32 (Z) grid system in the RVE. The grid distribution provided enough integration points to analyze the strain distribution in the central grain of the RVE [5]. Figure 1 shows the sectioned views of the simulation geometry. A defect containing polycrystal and the central defective grain are shown in Figure 1 (a-b), respectively.

The orientation of the central grain was fixed in a way that the [111] crystallographic pole was aligned along the Z-axis. Diagonal loading was applied in the RVE during the cyclic loading, i.e., along line $X = -Z$ and $Y = 0$. The rest of 23 grains, neighboring the large central grain, comprised of random orientation. The middle plane of the central grain was a (111) plane.

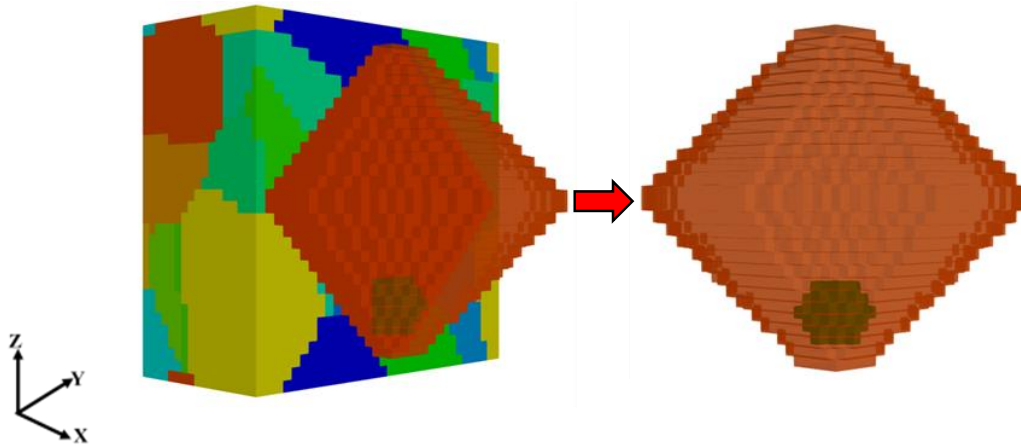


Figure 1. Cutaway views of a simulated geometry containing a defect.

Each of the RVE was simulated under fully reversed cyclic loading with strain amplitude of 0.012 mm/mm for 50 cycles. The material response was post-processed and analyzed after the simulations were completed to study the strain localization and crack initiation.

The methodology developed by Dodaran et al. [6] was followed to visualize the cyclic strain localization and crack initiation behavior. Binning analysis was performed on parallel crystallographic slip planes in the central grain of the RVE. Dodaran et al. [6] observed that strain localization was prominent on the (111) slip plane when the RVE was oriented along the Z-axis and loaded diagonally. Akin to that, the central grain was sliced into 28 equal parts, parallel to the (111) slip plane of IN718 (FCC matrix), and the thickness of each slice was one voxel.

At the peak of each loading cycle, the average of the von Mises strain of all voxels within a slice were calculated. PSBs were said to form in a section if the peak von Mises strain exceeded 0.02 mm/mm in more than half of voxels in any cycle. The area fraction of all the 28 slices were then calculated for the corresponding simulation cycle.

The difference in area fraction was calculated to capture the location and cycle of crack initiation. The PSB-matrix interfaces, which are the primary location of the crack initiation [9], was identified by the significant difference in the area fraction between the neighboring slices in the central grain. A 25% difference in the area fractions between the neighboring sections was set as a criterion to detect crack initiation.

Dodaran et al. [6] reported that the presence of a defect did not change the crack initiation mechanism unless the defect size was sufficiently large enough relative to grain size, i.e., 17.5 μm . A defect of identical shape and size were incorporated at three different locations in the center plane of the large central grain, i.e., $X = Y$, by varying the coordinates along the Z direction, as depicted in Figure 2. It is worth mentioning that each simulation geometry contains a single defect. The relative shift in the defect location is pictorially presented in Figure 2. The details of all the simulations performed in this study are reported in Table 2.

Table 2. Summary of all simulations of cyclic loading of defect containing polycrystalline aggregate performed in this study. Individual cases are shown with tick marks and corresponding case numbers inside parenthesis.

(X, Y, Z)		
(17, 17, 7)	(17, 17, 12)	(17, 17, 17)
✓(1)	✓(2)	✓(3)

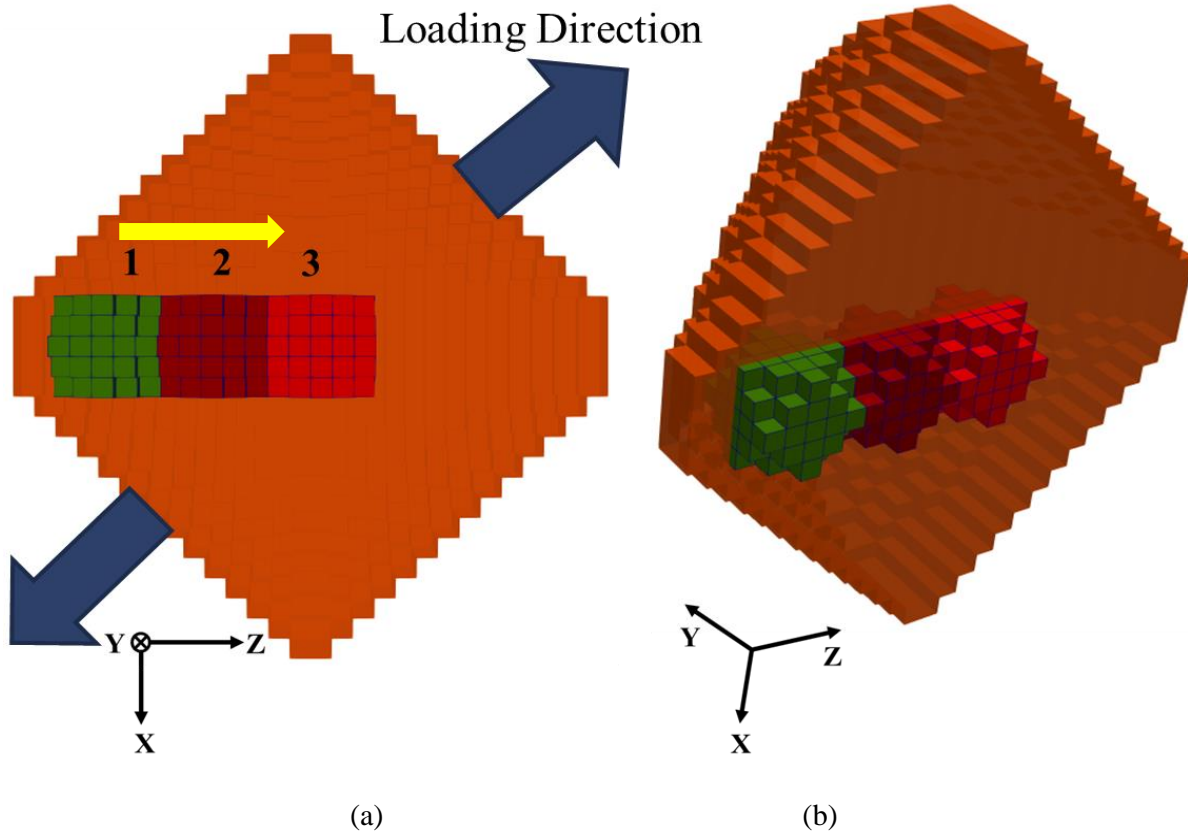


Figure 2. Illustration of the location of the defects in the central grain: (a) cross-sectional view of the central grain showing the defect with the associated case number and a yellow arrow indicating the change in defect position, (b) an angled sectional view to portray the defect shape.

Results and Discussions

Effect of defect location on strain localization and crack initiation

The presence of large defects imposes stress concentration in large material volume on the surrounding microstructure. This can affect the strain localization behavior and the subsequent crack initiation. This study primarily focuses on the effect of defect location, rather than shape/size, on the strain localization and crack formation mechanism.

To shed light on the strain localization behavior, three dimensional von Mises strain distribution at the peak of a loading cycle is presented in Figure 3 for all the simulations. The spatial distribution of the von Mises strain corresponds to the cycle mentioned in Table 3 at which the strain localization becomes evident. The central grains were marked by black dashed lines. It can be seen, as the defect moved closer to the middle plane of the central grain, the strain localization became more pronounced and occurred over a narrower region. In Figure 3(c), high strain localization is visible by regions in the boxed area, and the middle plane of the central grain corresponds to (111) plane. As reported by Dodaran et al. [6], this strain localization was likely caused due to large FSD value at the boxed region with low initial slip resistance and subsequent softening during the cyclic loading.

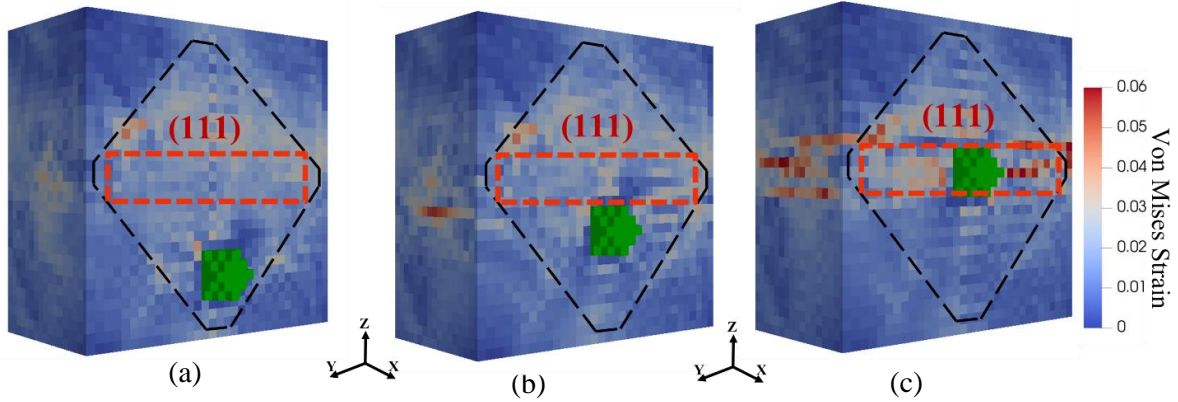


Figure 3. Three-dimensional von Mises strain distribution for three simulation cases shown in **Table 2** in ascending order. The volumes corresponding to the defects are colored in green. Boundaries of the central grain are marked using black dashed lines.

The investigate the crack initiation mechanism, the area fraction of the individual slices, that achieved von Mises strain greater than 0.02 at the peak of the loading cycle, were calculated in the central grain along the (111) plane. The area fraction was calculated for a particular cycle that had maximum number of slices achieving peak von Mises strain greater than 0.02 in half of the voxels within each slice and are presented in Figure 4 (a-c). Schematics of the volumetric defects are also shown in Figure 4 (a-f). The distribution of peak von Mises strain does not appear to be significantly affected by the presence of defects unless the defect is in close proximity of the middle plane in the central grain.

Table 3. Locations and simulated cycles to crack initiation (N_i), diagonally loaded specimen. The IDs of the simulation cases were also noted in the table.

(X, Y, Z)		
(17, 17, 7)	(17, 17, 12)	(17, 17, 17)
#1:26	#2: 26	#3: 23

From Figure 4 (a & b), it can be seen that when the defect is away from the middle plane of the central grain, the location with maximum area fraction with von Mises strain 0.02 first occurred at slice 20. The location shifted towards the pore, i.e., slice 15, when the defect moved closer to the middle plane as shown in Figure 4(c). The location and cycle of crack initiation can be determined from the difference in area fraction between the consecutive slices and shown in Figure 4 (d-f). The location of crack initiation can be identified by the sharp change in the area fractions between

consecutive slices. When the defects were away from the middle plane crack initiated between slice 20 and 21 for cases #1 and #2. The crack initiation location moved closer to the pore from slice 20 to around slice 15 of the central grain for case #3. The crack initiation cycle also followed a similar trend, i.e., ~26 simulation cycles for cases #1 and #2 while it reduced to 23 for case #3 and reported in Table 3. So, when defects are in close proximity of middle plane in the central grain, earlier crack initiation happen at the grain interior and the material would fail early.

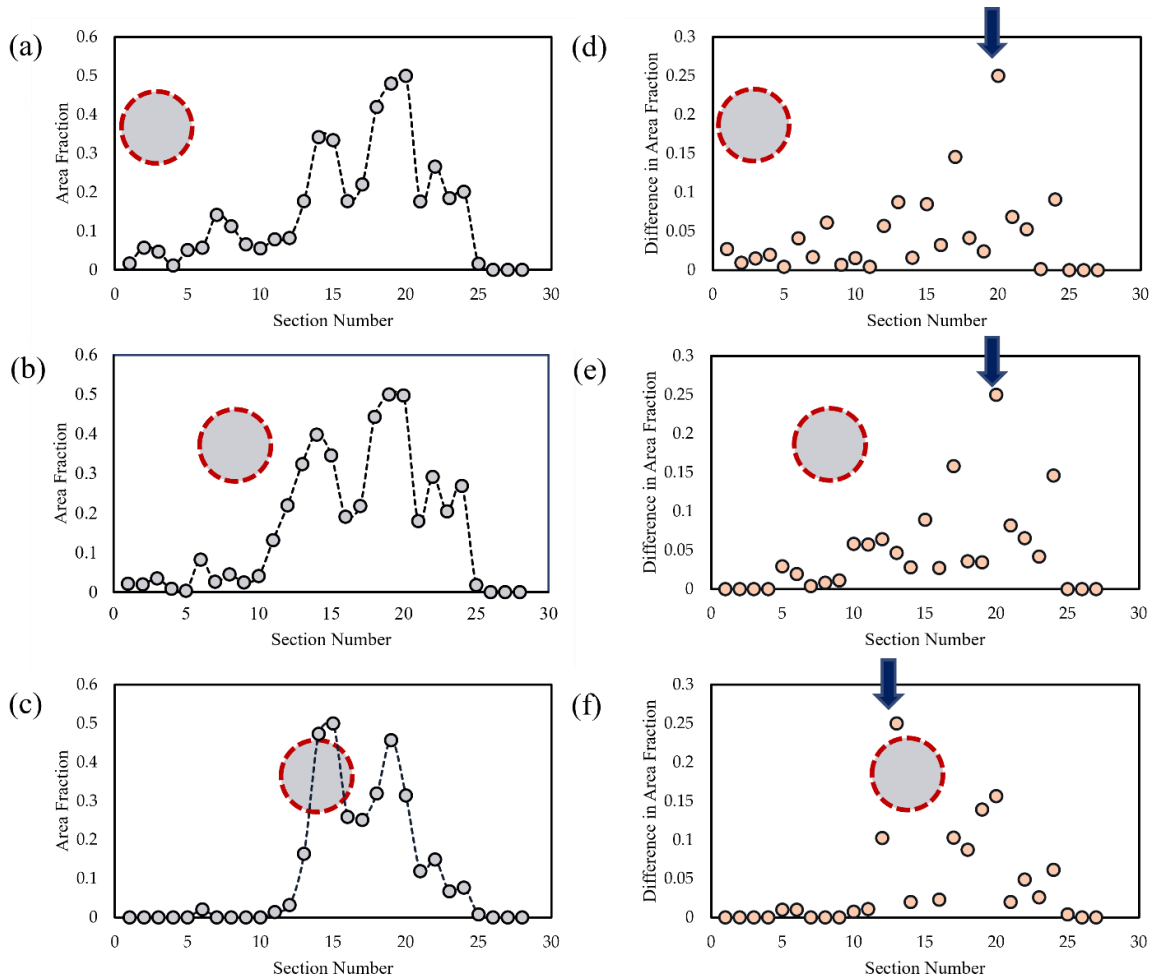


Figure 4. (a-c) Profiles of area fraction of all 28 slices along the (111) plane of the center grain for all the simulation cases with an average peak von Mises strain greater than 0.02 mm/mm. (d-f) the difference in area fraction of the consecutive slices in the central grain. Panels (a, d), (b, e), (c, f) respectively represent the simulation results for three different defect location.

Conclusion

In this study, CP simulations were performed to investigate the effect of defect location on the fatigue crack initiation mechanism for laser powder bed fused (L-PBF) IN718. The strain localization and crack initiation behavior were explored as a function of defect location in the central grain of the polycrystalline aggregate. The following conclusions were drawn:

- The strain localization in the middle plane of the central grain increased as the defect shifted closer to middle plane.

- The location of defects did not affect the crack initiation mechanism until the defects were near the middle plane.
- As the defects moved closer to the middle plane of the central grain, the crack initiation cycle reduced and the location of PSBs formation, and crack initiation shifted toward the defect.

Acknowledgment

This article is based upon work partially supported by the U.S. National Aeronautics and Space Administration (NASA) under Award No. 80NSSC21M0361. This paper describes objective technical results and analysis. Any subjective views or opinions that might be expressed in the paper do not necessarily represent the views of the NASA or the United States Government.

References

- [1] Mostafaei A, Zhao C, He Y, Reza Ghiaasiaan S, Shi B, Shao S, et al. Defects and anomalies in powder bed fusion metal additive manufacturing. *Curr Opin Solid State Mater Sci* 2022;26:100974. <https://doi.org/10.1016/j.cossms.2021.100974>.
- [2] Nezhadfar PD, Johnson AS, Shamsaei N. Fatigue behavior and microstructural evolution of additively manufactured Inconel 718 under cyclic loading at elevated temperature. *Int J Fatigue* 2020;136:105598. <https://doi.org/10.1016/j.ijfatigue.2020.105598>.
- [3] Wan H-Y, Zhou Z-J, Li C-P, Chen G-F, Zhang G-P. Enhancing Fatigue Strength of Selective Laser Melting-Fabricated Inconel 718 by Tailoring Heat Treatment Route. *Adv Eng Mater* 2018;20:1800307. <https://doi.org/https://doi.org/10.1002/adem.201800307>.
- [4] Yang K, Huang Q, Wang Q, Chen Q. Competing crack initiation behaviors of a laser additively manufactured nickel-based superalloy in high and very high cycle fatigue regimes. *Int J Fatigue* 2020;136:105580. <https://doi.org/10.1016/j.ijfatigue.2020.105580>.
- [5] Muhammad M, Frye P, Simsiriwong J, Shao S, Shamsaei N. An investigation into the effects of cyclic strain rate on the high cycle and very high cycle fatigue behaviors of wrought and additively manufactured Inconel 718. *Int J Fatigue* 2021;144:106038. <https://doi.org/10.1016/j.ijfatigue.2020.106038>.
- [6] Dodaran MS, Muhammad M, Shamsaei N, Shao S. Synergistic Effect of Microstructure and Defects on the Initiation of Fatigue Cracks in Additively Manufactured Inconel 718. *Int J Fatigue* 2022:107002. <https://doi.org/10.1016/J.IJFATIGUE.2022.107002>.
- [7] Roters F, Diehl M, Shanthraj P, Eisenlohr P, Reuber C, Wong SL, et al. DAMASK – The Düsseldorf Advanced Material Simulation Kit for modeling multi-physics crystal plasticity, thermal, and damage phenomena from the single crystal up to the component scale. *Comput Mater Sci* 2019;158:420–78. <https://doi.org/10.1016/j.commatsci.2018.04.030>.
- [8] Hennessey C, Castelluccio GM, McDowell DL. Sensitivity of polycrystal plasticity to slip system kinematic hardening laws for Al 7075-T6. *Mater Sci Eng A* 2017;687:241–8. <https://doi.org/10.1016/j.msea.2017.01.070>.
- [9] Polák J, Man J. Fatigue crack initiation - The role of point defects. *Int J Fatigue* 2014;65:18–27. <https://doi.org/10.1016/j.ijfatigue.2013.10.016>.